Shaken or Stirred: The Diffuse Interstellar Medium with Exceptionally High SiO Abundance

Daniel R Rybarczyk, Snežana Stanimirović, Antoine Gusdorf

The Astrophysical Journal, 950:52 (15pp), 2023 June 10 https://doi.org/10.3847/1538-4357/accba1

Shaken or Stirred: The Diffuse Interstellar Medium with Exceptionally High SiO Abundance

Daniel R. Rybarczyk[1], Snežana Stanimirović[1], and Antoine Gusdorf[2,3]
[1] University of Wisconsin–Madison, Department of Astronomy, 475 N. Charter St., Madison, WI 53703, USA; rybarczyk@astro.wisc.edu
[2] Laboratoire de Physique de l'École Normale Supérieure, ENS, Université PSL, CNRS, Sorbonne Université, Université de Paris, F-75005 Paris, France
[3] Observatoire de Paris, PSL University, Sorbonne Université, LERMA, F-75014 Paris, France
Received 2023 January 25; revised 2023 April 7; accepted 2023 April 8; published 2023 June 9

Abstract

Interstellar shocks, a key element of stellar feedback processes, shape the structure of the interstellar medium (ISM) and are essential for the chemistry, thermodynamics, and kinematics of interstellar gas. Powerful, high-velocity shocks are driven by stellar winds, young supernova explosions, more evolved supernova remnants, cloud–cloud collisions, and protostellar outflows, whereas the existence and origin of much-lower-velocity shocks ($\lesssim$10 km s^{-1}) are not understood. Direct observational evidence for interstellar shocks in diffuse and translucent ISM environments has been especially lacking. We present the most sensitive survey to date of SiO—often considered an unambiguous tracer of interstellar shocks—in absorption, obtained with the Northern Extended Millimeter Array interferometer. We detect SiO in five of eight directions probing diffuse and translucent environments without ongoing star formation. Our results demonstrate that SiO formation in the diffuse ISM (i.e., in the absence of significant star formation and stellar feedback) is more widespread and effective than previously reported. The observed SiO line widths are all $\lesssim$4 km s^{-1}, excluding high-velocity shocks as a formation mechanism. Yet, the SiO abundances we detect are mostly 1–2 orders of magnitude higher than those typically assumed in quiescent environments and are often accompanied by other molecular transitions whose column densities cannot be explained with UV-dominated chemical models. Our results challenge the traditional view of SiO production via stellar feedback sources and emphasize the need for observational constraints on the distribution of Si in the gas phase and grain mantles, which are crucial for understanding the physics of grain processing and the diffuse interstellar chemistry.

Unified Astronomy Thesaurus concepts: Diffuse molecular clouds (381); Interstellar line absorption (843); Shocks (2086)

1. Introduction

Shocks generated by various forms of stellar feedback play a pivotal role in galaxy evolution (McKee & Ostriker 1977; Hopkins et al. 2012). Spectral line observations of the SiO molecule have provided a key tool for identifying possible feedback sources based on the abundances of SiO and the shock velocities. Shocks can enhance the SiO abundance, $X_{\rm SiO} = N({\rm SiO})/N({\rm H_2})$, by up to 6 orders of magnitude relative to quiescent environments (Martin-Pintado et al. 1992; Amo-Baladrón et al. 2011; López-Sepulcre et al. 2016; Yu et al. 2018; Li et al. 2019; Armijos-Abendaño et al. 2020). High-velocity ($v \gtrsim 25$ km s^{-1}) shocks caused by supernova remnants, large-scale cloud collisions, expanding H II regions, or protostellar outflows are known to be highly effective at forming SiO (Martín-Pintado et al. 1997; Gueth et al. 1998; Hatchell et al. 2001; Gusdorf et al. 2008) by extracting Si from the dust grains, which then reacts with either O_2 or OH to form SiO (Herbst et al. 1989; Schilke & Walmsley 1997). Recent observations, though, have provided surprising evidence for the existence and effectiveness of low-velocity shocks ($v \lesssim 15$ km s^{-1}) in forming SiO in dense interstellar environments (Jiménez-Serra et al. 2010; Nguyen-Lu'o'ng et al. 2013; Duarte-Cabral et al. 2014; López-Sepulcre et al. 2016; Louvet et al. 2016; De Simone et al. 2022). The origin of these low-velocity shocks remains poorly constrained, although possible explanations include converging flows (Jiménez-Serra et al. 2010), cloud collisions (Louvet et al. 2016), decelerated protostellar shocks from no-longer-active star formation events (López-Sepulcre et al. 2016), and trains of shocks formed at the boundary of an expanding bubble (De Simone et al. 2022).

Observational measurements of SiO abundances are also important for constraining details of the dust grain physics. While it is understood that most of the Si in the interstellar medium (ISM) is locked inside the dust grain cores (Jenkins 2009), the amount of Si that is either free in the gas-phase ISM or located in the mantles of dust grains is currently poorly constrained, yet affects greatly many astrochemical reactions. For example, modeling suggests that if 1%–10% of silicon is present in the gas phase, then SiO column densities produced in low-velocity shocks can be several orders of magnitude higher than in environments where Si is entirely locked in grain cores and mantles (Nguyen-Lu'o'ng et al. 2013; Louvet et al. 2016).

Shocks produced by stellar feedback predominantly shape dense environments, most of which are star-forming. Meanwhile, in more diffuse environments without ongoing star formation to provide such feedback, chemical abundances have been puzzling for many years. Standard astrochemical models have not been able to explain the high abundances of many species (HCO^+, HCN, and C_2H, among others) in the diffuse ISM, leading to the hypothesis that turbulence, and in the most extreme cases shocks, could be responsible for the high abundances (e.g., Godard et al. 2009, 2010; Reach & Heiles 2021; Rybarczyk et al. 2022a). Yet, direct observations of shock tracers like SiO in the diffuse ($A_V \lesssim 1$) and translucent

Table 1
The Background Radio Continuum Sources against Which We Measured Absorption in This Work

Source	ℓ (deg)	b (deg)	F_{90} (Jy)	$\sigma_{l/c}$	A_V (mag)
2023+335	73.1	−2.4	1.01	0.001	5.21
3C 418	88.8	6.0	1.00	0.001	3.18
3C 111A	161.7	−8.8	1.14	0.002	4.41†
BL Lac	92.6	−10.4	2.10	0.001	1.22
NRAO 530	12.0	10.8	1.97	0.003	1.52
4C 09.57	34.9	17.6	2.24	0.003	0.47
4C+28.07	149.5	−28.5	0.97	0.002	0.45
J0423-0120	195.3	−33.1	3.69	0.001	0.42

Notes. We list the name of the continuum source (column (1)); the Galactic longitude, ℓ (column (2)); the Galactic latitude, b (column (3)); the 90 GHz flux density of the background source, F_{90} (column (4)); the noise in the line divided by the continuum ($\sim\sigma_{l/c}$; column (5)); and the visual extinction along the line of sight, A_V (column (6)). All A_V values are derived from Planck Collaboration et al. (2016b) except that for 3C 111A, indicated with a †, which is derived from the higher-resolution map of California made with Herschel by Lada et al. (2017).

($1 \lesssim A_V \lesssim 4$) ISM are extremely rare (Lucas & Liszt 2000; Corby et al. 2018).

In this work, we search for SiO in absorption against eight background radio continuum sources at 3 mm wavelength in the direction of diffuse and translucent gas in the Milky Way with the Northern Extended Millimeter Array (NOEMA). We also observe HCO^+ in absorption in these directions to trace the total quantity of molecular gas. The observations are described in Section 2. In Section 3 we present the methods for decomposing absorption spectra into Gaussian components and calculating the column densities of different molecular species. We then characterize the observed environments using new and existing data in the direction of our background radio continuum sources. In Section 5, we report the SiO column densities and abundances in these diffuse and translucent environments. We discuss these results in Section 6, both in the context of diffuse interstellar chemistry and in the context of existing literature. We then present our conclusions in Section 7.

2. Observations

We searched for SiO ($J = 2$–1, 86.8470 GHz) and HCO^+ ($J = 1$–0, 89.1885 GHz) in absorption with NOEMA (projects W19AQ, S20AB, and E20AA) in the direction of eight background radio continuum sources, probing diffuse and translucent environments (Table 1; Figure 1). The sources were observed for a total of 1.1–11.8 hr (including overheads, spanning one to five sets of observations) to reach a targeted optical depth sensitivity of ≈0.002 (see Table 1 for the achieved sensitivities). The bright quasars 3C 84, 3C 454.3, 3C 345, 0059+581, 3C 723, and 3C 279 were used as bandpass calibrators; the bandpass was stable over the 0.9–5.1 hr observed in each set of observations. Both lines were placed in high-resolution chunks (62.5 kHz channel spacing ≈0.2 km s^{-1} velocity spacing) in the lower side band to achieve the optimal sensitivity. We carried out standard calibration using the CLIC and MAPPING software, part of the GILDAS software collection[4] (Pety 2005; Gildas Team 2013). Because our background sources were bright ($\gtrsim$1 Jy; Table 1), we further performed self-calibration using the 2020 self-calibration tool in MAPPING on all sources. The final spectra presented in Figure 2 were smoothed to a 0.4 km s^{-1} velocity resolution. Table 1 lists the noise in the line divided by the continuum ($e^{-\tau(v)}$) for reference (the noise levels in the HCO^+ and SiO spectra are very similar). In the direction of 3C 111, where the HCO^+ absorption is saturated, we also utilized observations of $H^{13}CO^+$ ($J = 1$–0, 86.7543 GHz) from NOEMA obtained in the same observing run of the HCO^+ observations (project W19AQ), achieving comparable sensitivity.

[4] https://www.iram.fr/IRAMFR/GILDAS

3. SiO and HCO^+ in the Diffuse ISM

We detect HCO^+ in absorption in all eight directions and we detect SiO in absorption in five of the eight directions in our sample. In Figure 2 we show the observed SiO and HCO^+ absorption spectra with Gaussian fits; Table 2 lists all 31 HCO^+ Gaussian absorption components and all eight SiO Gaussian absorption components (see Section 3.1). Three of the absorbing structures are located within 500 pc, while the remaining five are at a distance of 1–2 kpc, as illustrated in Figure 1 (see Section 4). Because HCO^+ absorption in the direction of 3C 111A is saturated, we also utilize $H^{13}CO^+$ observations from NOEMA in this direction (Lucas 1998); the $H^{13}CO^+$ spectrum is shown in Figure 2 and the Gaussian fits are listed in Table 2.

3.1. Gaussian Decomposition

We decompose all absorption spectra in this work into Gaussian components. For each spectrum, we supply initial guesses for the number of components as well as for the amplitude, FWHM, and central velocity of each component. We then use Python's `scipy.optimize.curve_fit` to fit the Gaussian components to the spectrum. To obtain the final estimates and uncertainties, we refit the spectra with Gaussian components over 1000 trials, adding random noise to the spectrum in each trial. We take the mean and standard deviation over all trials to be the estimate and uncertainty for each fitted quantity (the amplitude, FWHM, and central velocity of each Gaussian component).

We use the same initial guesses for the number of components and the central velocities of the components in the HCO^+ and SiO absorption spectra. The number of components is determined by inspection of the HCO^+ absorption spectrum for each sight line, which assumes that any structures observed in SiO are also observed in HCO^+ (visual inspection clearly shows that all peaks in SiO absorption are coincident with peaks in HCO^+ absorption; moreover, previous observations confirm HCO^+ is present where SiO is observed; Lucas & Liszt 2000; López-Sepulcre et al. 2016). We then reject components detected at a level $<3\sigma$. The only exception is the case of NRAO 530, where the peak in the SiO absorption is detected only at a level of 2.2σ, while the integrated absorption ($\int\tau(v)dv$) is detected at 2.7σ. Both metrics suggest that this is only a marginal detection. Yet, because the peak in the SiO absorption is coincident with the peak in the HCO^+ absorption and because previous work has revealed excess SiO absorption toward NRAO 530 at ∼5 km s^{-1} (see Section 3.5; Lucas & Liszt 2000), we classify this feature as a detection. All of the Gaussian fits are shown in Figure 2 and listed in Table 2. In

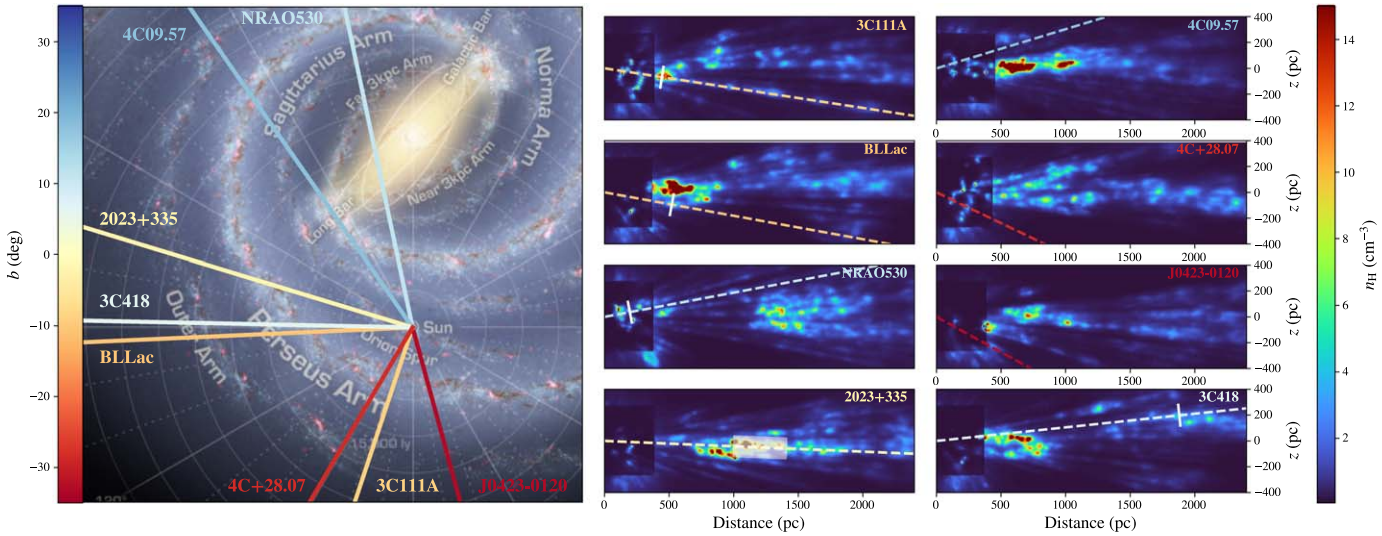

Figure 1. An overview of the sight lines observed in this work. Left: Artist's conception of the Milky Way, with prominent features labeled (credit: NASA/JPL-Caltech/R. Hurt, SSC-Caltech). The directions of our extragalactic background sources are shown, colored according to Galactic latitude. Right: Cross sections through the Lallement et al. (2019) and Leike et al. (2020) 3D dust maps of the local ISM. Both maps are shown with the same density scale; the peak density shown is 15 cm^{-3}, but peak densities in the maps reach as high as 63 cm^{-3}. The higher-resolution Leike et al. (2020) map, visible at the shortest distances, is plotted over the lower-resolution Lallement et al. (2019) map. Due to the varying resolutions and methods for measuring n_H, the densities may be discrepant between the two maps. The directions to our background sources are shown in dashed lines, colored by latitude, as in the left figure. The peak density in the direction of our background sources is 25 cm^{-3}. White lines are drawn perpendicular to the sight lines to indicate the estimated positions where SiO absorption is detected. For 2023+335, we show a partially transparent box to indicate the rather large range of distances over which the SiO could presumably originate.

Section 3.4, we discuss the bias to X_{SiO} introduced by our Gaussian fitting.

HCO^+ absorption in the direction of 3C 111A is saturated, so the approach outlined above is potentially problematic. We therefore also fit Gaussian components to the (unsaturated) $H^{13}CO^+$ absorption spectrum. The $H^{13}CO^+$ absorption spectrum is shown in Figure 2 and the Gaussian components are listed in Table 2 (indicated with a superscript dagger). We estimate $N(HCO^+) = 61 \times N(H^{13}CO^+)$ based on previous observations of HCO^+ and HCN isotopologues in the direction of 3C 111 (Lucas 1998). The fitted $H^{13}CO^+$ absorption components have narrower line widths than their saturated HCO^+ counterparts, but the column densities vary by $\lesssim$30% when using $H^{13}CO^+$ compared to using just HCO^+, so they do not change any of the qualitative results presented in this work. The results presented in Section 5 are those derived from $H^{13}CO^+$, which we take to be more reliable. The uncertainties include the uncertainty in $N(HCO^+)/N(H^{13}CO^+)$.

3.2. Deriving Molecular Column Densities

For a transition from an upper state u to a lower state l observed in absorption, the column density, N, is given by

$$N = Q(T_{ex})\frac{8\pi\nu^3}{c^3}\frac{1}{g_u A_{ul}}[1 - \exp(-h\nu/kT_{ex})]^{-1}\int\tau(v)dv, \quad (1)$$

where T_{ex} is the excitation temperature (see Section 3.3), $Q(T_{ex})$ is the partition function, ν is the rest frequency of the transition, g_u is the degeneracy of the upper state, A_{ul} is the Einstein A coefficient for the transition, and $\tau(v)$ is the optical depth of the line at velocity v. We evaluate Equation (1) using the values given in the Cologne Database for Molecular Spectroscopy (Müller et al. 2001; Endres et al. 2016) and the Leiden Atomic and Molecular Database (Schöier et al. 2010). Results are listed in Table 3 for different excitation temperatures (in this work, we use $T_{ex} = 2.725$ K; see next section).

3.3. Excitation Temperatures

According to Equation (1), the excitation temperature is crucial for determining the column density from absorption measurements. For most molecular species in the diffuse and translucent ISM, T_{ex} is typically assumed to be equal to the temperature of the cosmic microwave background, 2.725 K (Lucas & Liszt 1996; Liszt 2001). Indeed, for sight lines where both the (2–1) and (1–0) or the (3–2) and (1–0) transitions of HCO^+ were observed in absorption, the HCO^+ excitation temperature was found to be equal to T_{CMB} within errors (Godard et al. 2010; Luo et al. 2020).

However, numerical simulations have shown that the HCO^+ excitation temperature may rise above T_{CMB} to ~4–5 K for densities 300 cm$^{-3} \lesssim n \lesssim 10^3$ cm^{-3} (Gong et al. 2020; Rybarczyk et al. 2022a). Such behavior could lead to the HCO^+ column densities being underestimated by a factor of ~2. Meanwhile, SiO excitation temperatures are usually thought to be higher than T_{CMB}, with estimates—and in some cases direct measurements—ranging within roughly 5–100 K, mostly within ~10–40 K (Jiménez-Serra et al. 2010; López-Sepulcre et al. 2016; Rivilla et al. 2018; Yu et al. 2018; Li et al. 2019; Armijos-Abendaño et al. 2020), but these are in environments of much higher density (10^4 cm$^{-3} \lesssim n \lesssim 10^7$ cm^{-3}) than probed by our observations.

In this work, we assume that the excitation temperature of HCO^+ is equal to T_{CMB}, to be consistent with previous work (Lucas & Liszt 1996; Liszt 2001; Liszt et al. 2014; Rybarczyk et al. 2022b) and with existing observations of different rotational transitions of HCO^+ (Godard et al. 2010; Luo et al. 2020), as well as the weakness of HCO^+ emission in these directions (Lucas & Liszt 1996 and Section 4.2). We also assume that the excitation temperature of SiO is equal to T_{CMB},

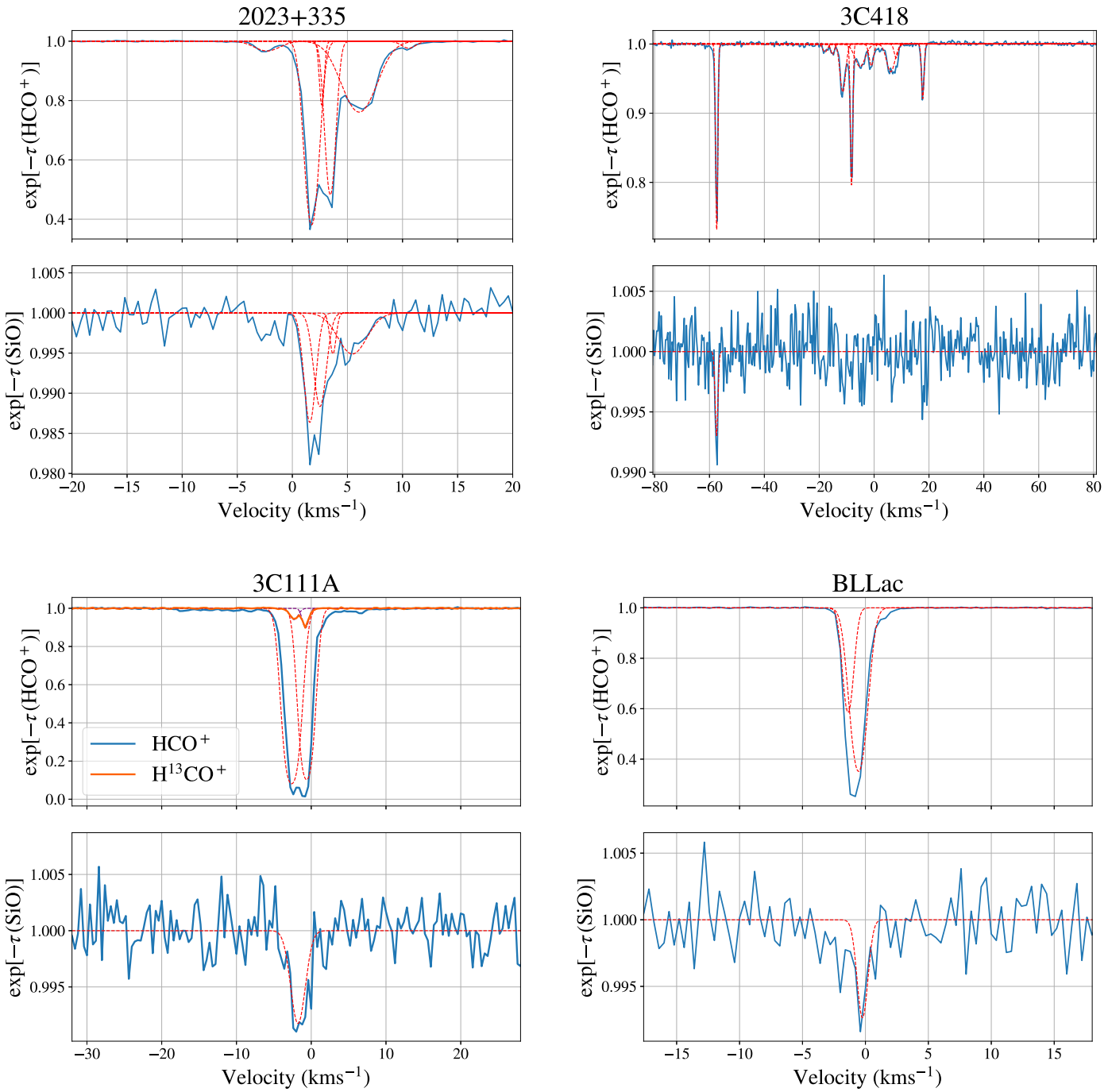

Figure 2. The HCO^+ (top) and SiO (bottom) absorption spectra ($e^{-\tau}$) in the direction of our eight background sources. Gaussian fits are shown as red dashed lines for both species. For 3C 111A, we also show the $H^{13}CO^+$ absorption spectra and Gaussian fits.

as suggested by the RADEX non-LTE molecular radiative transfer code (van der Tak et al. 2007) for the low densities in the directions of our background sources (see Section 4). Results for $T_{ex} = 4$ K and $T_{ex} = 5$ K are listed in Table 3 for reference.

3.4. Measuring N(H)$_2$ and SiO Abundances

For every component identified in SiO absorption, we measure the SiO abundance, $X_{SiO} = N(SiO)/N(H_2)$, where $N(H_2) \approx N(HCO^+)/3 \times 10^{-9}$ (e.g., Liszt & Lucas 2000; Liszt et al. 2010; see discussion below). $N(SiO)$ and $N(HCO^+)$ are solved using Equation (1) for the Gaussian components. There are multiple Gaussian HCO^+ absorption components identified along all lines of sight where SiO is detected in absorption. In order to isolate individual absorbing structures along the line of sight, we calculate X_{SiO} using the HCO^+ absorption component closest in velocity to each SiO absorption component.

Conversion from $N(HCO^+)$ to $N(H_2)$ is essential for calculating SiO abundances in this work. A large body of work using high-resolution interferometric observations exists and has confirmed a linear relationship between the HCO^+ and H_2 column densities in the diffuse/translucent medium (Liszt & Lucas 2000; Liszt et al. 2010), with recent results placing the

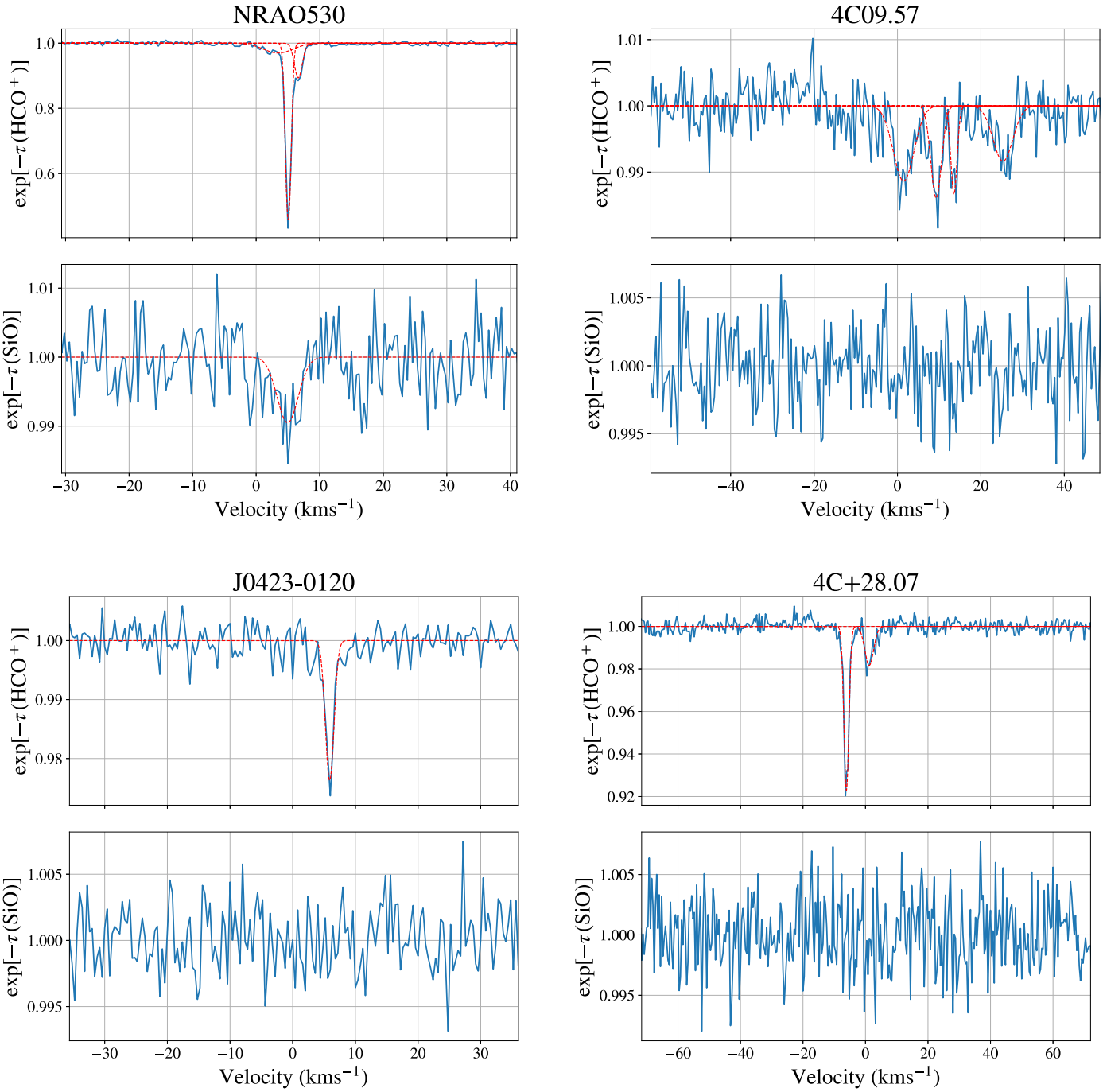

Figure 2. (Continued.)

conversion factor at $N(\mathrm{HCO^+})/N(\mathrm{H_2}) = 3 \times 10^{-9} \pm 0.21$ dex (Gerin et al. 2019; Liszt & Gerin 2023). We adopt this empirically derived result in this work. These estimates are derived from interferometric observations of $\mathrm{HCO^+}$ in absorption, which are superior to single-dish studies because they probe very small solid angles and trace even cold, weakly excited molecular gas that does not emit significant radiation. As a confirmation that this linear relation is well constrained, it has been shown that the column density of $\mathrm{H_2}$ inferred from $\mathrm{HCO^+}$ (using a conversion factor of 3×10^{-9}) could account for the difference between column densities derived from H I and CO (another proxy for $\mathrm{H_2}$) and those inferred from γ-rays and dust emission (considered to be unbiased tracers of the total column density; Liszt et al. 2018).

For all sight lines except that to 3C 418, there are $\geqslant 2$ $\mathrm{HCO^+}$ components at similar velocities to those where we see SiO absorption. This clearly introduces potential biases, as the calculation of X_{SiO} depends on our Gaussian decomposition (of both the SiO and the $\mathrm{HCO^+}$ spectra) as well as on our velocity matching. In order to quantify this bias, we also estimate X_{SiO} integrated over the total velocity range where SiO and $\mathrm{HCO^+}$ are observed, rather than just for the individual Gaussian components. We summarize these results in Table 4. For 3C 111A (using both $\mathrm{HCO^+}$ and $\mathrm{H^{13}CO^+}$), BL Lacertae (BL Lac),

Table 2
Gaussian Components Fitted to the HCO^+ and SiO Absorption Spectra

Sight Line	τ_{HCO^+}	v_{HCO^+}	Δv_{HCO^+}	τ_{SiO}	v_{SiO}	Δv_{SiO}
2023+335	0.965 ± 0.001	1.75 ± 0.00	1.40 ± 0.00	0.014 ± 0.001	1.59 ± 0.11	1.25 ± 0.17
	0.243 ± 0.003	2.67 ± 0.00	0.50 ± 0.00	0.012 ± 0.002	2.51 ± 0.12	1.35 ± 0.34
	0.729 ± 0.001	3.45 ± 0.00	1.05 ± 0.00	0.005 ± 0.001	3.68 ± 0.15	0.67 ± 0.19
	0.273 ± 0.001	6.07 ± 0.01	3.59 ± 0.01	0.005 ± 0.001	5.45 ± 0.04	3.07 ± 0.74
	0.024 ± 0.001	10.56 ± 0.03	1.50 ± 0.06	...	...	...
	0.033 ± 0.001	-2.30 ± 0.00	2.66 ± 0.00	...	...	...
	0.007 ± 0.001	-81.49 ± 0.17	2.63 ± 0.72	...	...	...
3C 111A	2.514 ± 0.003	-2.62 ± 0.01	2.18 ± 0.01	0.008 ± 0.002	-1.77 ± 0.16	2.30 ± 0.35
	$0.061 \pm 0.002^\dagger$	$-2.30 \pm 0.02^\dagger$	$1.29 \pm 0.07^\dagger$			
	2.280 ± 0.004	-0.62 ± 0.01	1.92 ± 0.01	...	...	...
	$0.108 \pm 0.002^\dagger$	$-0.76 \pm 0.01^\dagger$	$0.97 \pm 0.03^\dagger$			
3C 418	0.313 ± 0.001	-57.38 ± 0.00	0.91 ± 0.01	0.007 ± 0.002	-57.44 ± 0.10	1.20 ± 0.19
	0.012 ± 0.001	-17.86 ± 0.12	2.01 ± 0.32	...	...	...
	0.015 ± 0.001	-15.14 ± 0.08	1.49 ± 0.17	...	...	...
	0.072 ± 0.001	-11.41 ± 0.04	2.38 ± 0.10	...	...	...
	0.228 ± 0.004	-8.23 ± 0.00	0.98 ± 0.03	...	...	...
	0.033 ± 0.002	-5.14 ± 0.18	4.45 ± 0.99	...	...	...
	0.032 ± 0.002	-1.02 ± 0.04	1.89 ± 0.15	...	...	...
	0.041 ± 0.001	6.05 ± 0.07	3.54 ± 0.15	...	...	...
	0.020 ± 0.002	8.03 ± 0.06	1.65 ± 0.08	...	...	...
	0.082 ± 0.001	17.73 ± 0.01	1.06 ± 0.02	...	...	...
4C+28.07	0.080 ± 0.002	-6.10 ± 0.01	1.86 ± 0.03	...	...	...
	0.019 ± 0.002	1.18 ± 0.11	3.30 ± 0.33	...	...	...
4C 09.57	0.011 ± 0.003	1.47 ± 0.27	5.82 ± 1.60	...	...	...
	0.014 ± 0.003	9.27 ± 0.21	3.01 ± 0.73	...	...	...
	0.013 ± 0.003	13.54 ± 0.18	1.77 ± 0.27	...	...	...
	0.008 ± 0.003	25.29 ± 0.34	5.54 ± 1.55	...	...	...
BL Lac	0.536 ± 0.001	-1.38 ± 0.00	0.96 ± 0.01	...	...	...
	1.046 ± 0.002	-0.55 ± 0.00	1.45 ± 0.00	0.007 ± 0.002	-0.23 ± 0.16	1.01 ± 0.34
J0423-0120	0.024 ± 0.001	5.90 ± 0.03	1.62 ± 0.10	...	...	...
NRAO 530	0.780 ± 0.003	5.05 ± 0.00	0.96 ± 0.01	0.010 ± 0.004	4.96 ± 0.33	3.92 ± 1.13
	0.113 ± 0.003	6.63 ± 0.02	1.44 ± 0.05	...	...	...
	0.031 ± 0.003	3.47 ± 0.19	5.44 ± 0.45	...	...	...

Notes. The optical depth (τ), the FWHM (Δv), and the central velocity (v) of each component are listed for both molecular species. For 3C 111A, we also list results for the Gaussian decomposition of the $H^{13}CO^+$ spectrum, indicated with a † superscript.

Table 3
Conversions between the Column Density and Integrated Optical Depth for HCO^+ and SiO at Different Excitation Temperatures

T_{ex} (K)	$N/\int \tau_{HCO^+} dv$ (cm^{-2}/km s^{-1})	$N/\int \tau_{SiO} dv$ (cm^{-2}/km s^{-1})
2.725	1.09×10^{12}	3.45×10^{12}
4	1.77×10^{12}	5.53×10^{12}
5	2.44×10^{12}	7.53×10^{12}

Note. In this work, we use $T_{ex} = 2.725$ K (see discussion in Section 3.3).

Table 4
SiO Abundance Evaluated over the Entire Velocity Range Where Both SiO and HCO^+ Are Observed in Absorption and That Evaluated for Individual Gaussian Components

Sight Line	Velocity Range (km s^{-1})	X_{SiO} (Full Velocity Range) (10^{-10})	X_{SiO} (Gaussian Decomposition) (10^{-10})
2023+335	(−10, 20)	1.6	0.54, 1.6, 1.1, 10.5
3C 111A	(−10, 10)	$0.18^\dagger$	0.33
BL Lac	(−5, 5)	0.75	0.47
NRAO 530	(−5, 10)	4.5	4.7

Note. The value listed for 3C 111A is superscripted with † to indicate that this result is calculated using $H^{13}CO^+$ (the result, 0.18×10^{-10}, is the same if we use HCO^+).

and NRAO 530, X_{SiO} estimated over the entire velocity interval is within a factor of 2 of that estimated for the Gaussian components. There is a larger variation across 2023+335, although the Gaussian component with the highest estimated X_{SiO} accounts for only a small fraction of the total SiO and HCO^+ column densities along the line of sight, and the other three components are within a factor of 3 of X_{SiO} evaluated over the entire velocity range. Thus, our choice of Gaussian fits may bias our overall estimate of the SiO abundances along the diffuse and translucent lines of sight in our sample by a typical factor of <3. This does not meaningfully alter our conclusion that the SiO abundances we measure are significantly higher than those typically quoted for quiescent environments (Section 5).

3.5. Previous Observations

Several of these sight lines have been observed in SiO and HCO^+ absorption previously with lower sensitivity. Lucas & Liszt (2000) searched for SiO absorption in the direction of both 3C 111 ($\sigma_\tau \approx 0.007$) and NRAO 530 ($\sigma_\tau \approx 0.003$) at

$\sim$0.5 km s^{-1} velocity resolution. They reported significant detections in the integrated SiO optical depth for both sources, but their SiO absorption spectrum in the direction of 3C 111 showed no obvious peaks and could not be easily decomposed into Gaussian components. Moreover, more recent work by Liszt et al. (2014) did not detect SiO absorption in the direction of 3C 111 with better sensitivity ($\sigma_\tau \approx 0.005$) (albeit at lower velocity resolution $\sim$0.6 km s^{-1}). Lucas & Liszt (2000) reported a significant detection of SiO absorption in the direction of NRAO 530 around 5 km s^{-1}, where we find a marginal detection. SiO toward NRAO 530 was later confirmed with the Atacama Large Millimeter/submillimeter Array (ALMA) by Ando et al. (2016), though with only 3.4 km s^{-1} velocity resolution. Liszt et al. (2014) detected SiO toward BL Lac, but they did not discuss this result.

Earlier, Turner (1998) detected SiO in emission with very narrow line widths (<1 km s^{-1}) toward translucent molecular clouds. Yet, emission observations with single-dish telescopes have lower angular resolution relative to absorption (interferometric) studies and are less accurate in constraining SiO column density. The beam size in Turner (1998) was $\sim$74″, whereas we measure absorption against background continuum (point) sources unresolved at subarcsecond angular resolution. In addition, the structures observed by Turner (1998) all have estimated densities $>10^3$ cm^{-3} and visual extinctions $\gtrsim$3 mag (the visual extinction in that work, taken from model predictions for individual absorbing structures, represents a strict lower limit to the definition of visual extinction reported here in Table 1, which is taken directly from observations for the total line of sight; Planck Collaboration et al. 2016b). As noted in Lucas & Liszt (2000), the translucent structures probed by Turner (1998) in narrow-line SiO emission are probably significantly denser than most of the structures probed by narrow-line SiO absorption in directions with $A_V \lesssim$ a few magnitudes in this work. Moreover, four of the six directions where Turner (1998) detected SiO emission were at $|b| \leqslant 3\overset{\circ}{.}5$, whereas four of the five directions where we detect SiO in absorption are at $|b| > 6°$.

HCO^+ has been studied extensively in surveys of molecular absorption in the diffuse ISM. The sources 3C 111, NRAO 530, BL Lac, and 3C 418 have previously been observed in HCO^+ absorption (de Geus & Phillips 1996; Lucas & Liszt 1996). HCO^+ absorption profiles are stable over periods of a few years to a few tens of years (Wiklind & Combes 1997; Liszt & Lucas 2000; Han et al. 2017; Rybarczyk et al. 2022b). Our absorption profiles are consistent with previous observations in these directions, and are among the most sensitive in any of these directions.

4. Localizing Absorbing Structures

We use two recently constructed 3D dust maps (Lallement et al. 2019; Leike et al. 2020) to attempt to identify the specific gas structures we detect in absorption (Section 4.1). Given the spatial resolution (1–5 pc), we do not consider the volume densities reported in these maps, but instead only use these maps to identify absorbing structures along the line of sight. Figure 1 shows the directions we observe relative to prominent Galactic structures (left panel), as well as cross sections through the 3D dust maps in the direction of each background source. Table 5 lists the distance at which the peak density is measured in each map (see discussion below). After using these dust maps—as well as H I (HI4PI Collaboration et al. 2016) and CO (Dame et al. 2001; Dame & Thaddeus 2022)—to identify the absorbing structures, we also find estimates from the literature for the true volume densities of specific absorbing clouds (Section 4.2; Table 5). We discuss these observations on a source-by-source basis below.

Table 5
Summary of the Estimated Densities of Gas Structures along the Lines of Sight Observed in This Work

Source	$n_{\max}$ Dist. (L20) (pc)	$n_{\max}$ Dist. (L19) (pc)	$n_{\rm est}$ (cm^{-3})
3C 111A	276	505	10^2–a few $\times 10^3$
BL Lac	164	530	10^2–10^3
NRAO 530	199	185	$<10^3$
4C 09.57	147	160	$\lesssim$500
J0423-0120	144	165	$\lesssim$500
2023+335	27	1110	$\lesssim 10^3$
3C 418	361	355	$\lesssim 10^3$
3C 418–Perseus	⋯	1890	$\lesssim$200
4C+28.07	263	255	$\lesssim$500

Note. For each background source (column (1)), we list the distance of the density peak in the 3D dust maps from Lallement et al. (2019) ("L19") and Leike et al. (2020) ("L20") (columns (3) and (2), respectively). Finally, we list the estimated range of densities $n_{\rm est}$ for absorbing structures along the line of sight based on available literature and observations.

4.1. Distance Constraints Using 3D Dust Data

4.1.1. 3C 111

We see two HCO^+ absorption components in the direction of 3C 111, both associated with the California molecular cloud. California has an exceptionally low star formation rate for a cloud its size, and this sight line is not near any known young stellar objects (Lada et al. 2010, 2017), which can drive powerful shocks.

As confirmed in the detailed 3D map of California recently constructed by Rezaei Kh. & Kainulainen (2022), this cloud complex comprises an extended sheetlike structure and a bubble $\sim$25 pc in radius, which lies at the eastern edge of the molecular cloud. We find that the -2.5 km s^{-1} feature is associated with the shell of the eastern component, while the -1 km s^{-1} feature is associated with the western sheetlike component. This is evident in the moment map and channel maps shown in Figure 3, which show the boundary of the shell identified by Rezaei Kh. & Kainulainen (2022). In the density profile from the Lallement et al. (2019) map, there are two clear peaks around California in this direction—the eastern (bubble) component is nearer, at a distance of $\sim$450 pc, while the western (sheetlike) component is farther, at a distance of $\sim$500 pc. The SiO absorption that we fit appears to be associated with the eastern bubble component around -2.5 km s^{-1}. We note that it is possible to derive a two-component fit to the SiO absorption with residuals similar to those for the single-component fit. In this case, we would have SiO associated with both the bubble and the sheet component of California. The estimate of $X_{\rm SiO}$ would change only by a factor of $\sim$2 in this case from the single-component fit.

4.1.2. 2023+335

Being our lowest-latitude background source, the sight line toward 2023+335 is very complex. We detect seven

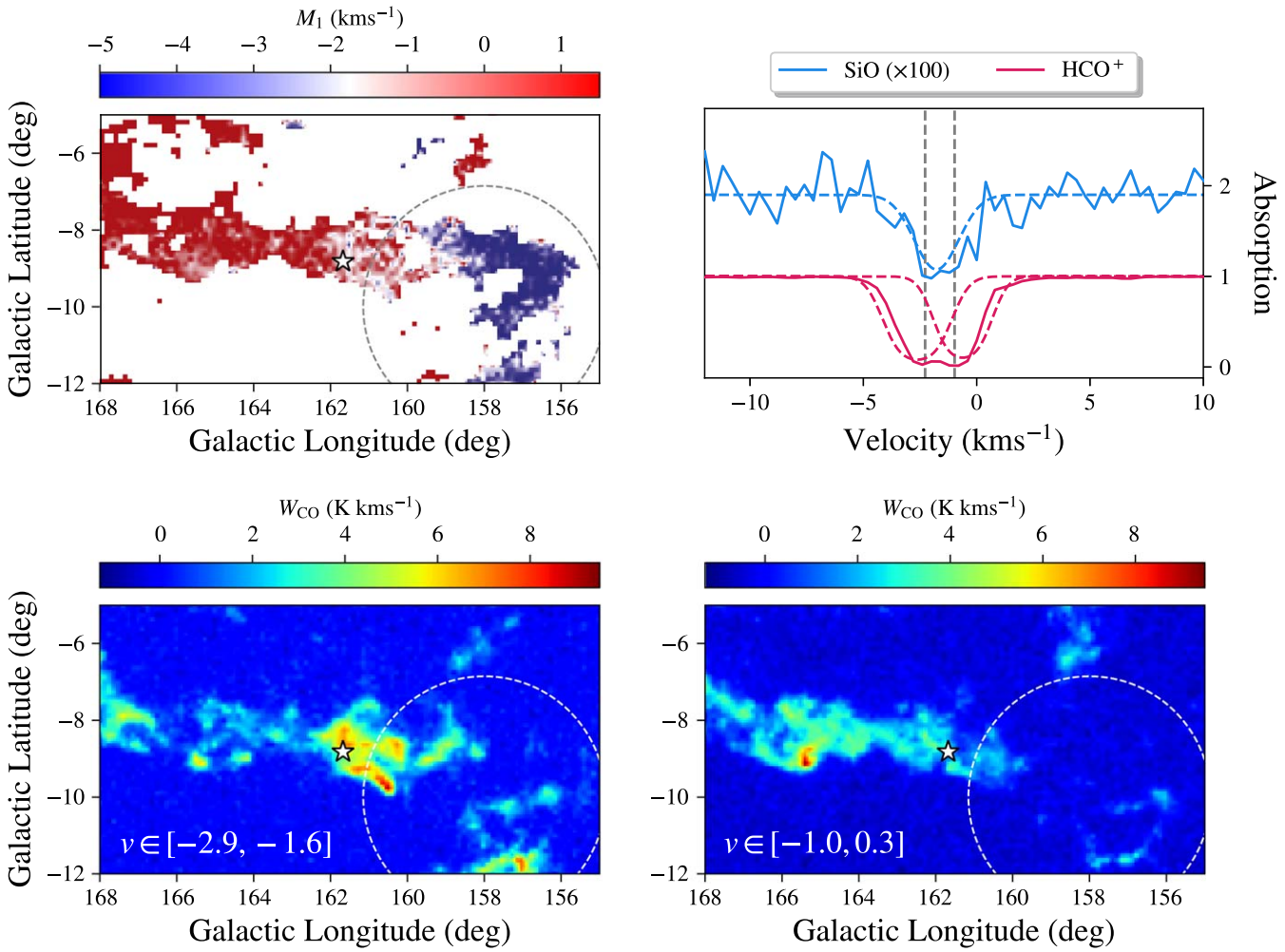

Figure 3. Top left: Moment 1 map of the California molecular cloud seen in CO emission (Dame et al. 2001). Top right: SiO and HCO^+ absorption spectra ($e^{-\tau}$) in the direction of 3C 111A. The SiO spectrum has been amplified by a factor of 100. Bottom left: Integrated CO emission from −2.9 to −1.6 km s^{-1} (Dame et al. 2001), the interval being roughly coincident with one of our HCO^+ absorption components and our SiO absorption component. Bottom right: Integrated CO emission from −1.0 to 0.3 km s^{-1} (Dame et al. 2001), the interval being roughly coincident with the other HCO^+ absorption component. In the moment 1 and integrated emission maps, the rough boundary of the bubble (Rezaei Kh. & Kainulainen 2022) in California is shown as a dashed line. The position of 3C 111A is shown as a white star. The ∼−2.5 km s^{-1} component appears to be mainly associated with this eastern bubble component of the California molecular cloud, whereas the CO emission associated with the lower-velocity components is mainly associated with the western sheetlike component of the cloud.

components in HCO^+ absorption and four components in SiO absorption. Nearly all of this absorption is detected between −5 and 10 km s^{-1}, associated with the Cygnus molecular cloud complex. As is evident in Figure 1, there are many density peaks along the line of sight. Determining the distances to all of the structures seen in HCO^+ absorption is complex and beyond the scope of this work, but most of this absorption lies between 700 and 1500 pc, as indicated by the semitransparent band in Figure 1.

4.1.3. 3C 418

There are nine HCO^+ absorption components in the direction of 3C 418 with velocities $-20 \text{ km s}^{-1} \lesssim v \lesssim 20 \text{ km s}^{-1}$. Most of these are likely associated with Cygnus—this sight line intersects the outskirts of the OB association Cyg OB7—although there are many density peaks along the line of sight, and determining the distances to all of the structures seen in HCO^+ absorption is complex and beyond the scope of this work. No SiO is detected at these velocities.

Meanwhile, the −57 km s^{-1} feature—where we detect a single component of both HCO^+ and SiO—is easily identified with the Perseus arm of the Galaxy at a distance of ∼1.9 kpc. If we isolate the higher-velocity gas in this direction, we can estimate A_V for the Perseus arm, $(N(\text{H I})_{\text{Per}} + 2N(\text{H}_2)_{\text{Per}})/(2.08 \times 10^{21} \text{ cm}^{-2}/\text{mag})$ (Zhu et al. 2017), where $N(\text{H I})_{\text{Per}}$ and $N(\text{H}_2)_{\text{Per}}$ are the H I and H_2 (derived from HCO^+) column densities calculated for the velocity interval including Perseus. Taking an extremely conservative interval, say, $-150 \text{ km s}^{-1} \lesssim v \lesssim -45 \text{ km s}^{-1}$, we find $A_V \lesssim 0.63$ for the Perseus arm. This is a strict upper limit—if we take a tighter interval that seems to trace the gas around our HCO^+ and SiO absorption, say, $-75 \text{ km s}^{-1} \lesssim v \lesssim -45 \text{ km s}^{-1}$, we find $A_V \approx 0.34$. This is the most diffuse environment where we detect SiO and, to our knowledge, the most diffuse environment where SiO has been detected in the ISM.

de Geus & Phillips (1996) searched for the (1–0) lines of both HCO^+ and CO in absorption toward 3C 418, detecting HCO^+ but not CO (the CO absorption spectrum had a sensitivity $\sigma_\tau \approx 0.2$ at 0.32 km s^{-1} velocity resolution). CO

was not detected in emission at these velocities in the survey of Dame et al. (2001) ($\sigma_{T_B} \approx 0.2$ K).

4.1.4. BL Lac

BL Lac is in the direction of the Lacerta molecular cloud, but not particularly near Lac OB1 or LBN 437, which is modified by Lac OB1 (Chen & Lee 2008). The direction toward BL Lac intersects the eastern part of an arc-like structure associated with Lacerta. As shown in Figure 4, this arc is visible in both the dust (e.g., Planck Collaboration et al. 2016b) and CO (Dame & Thaddeus 2022). It is clear from an inspection of the Lallement et al. (2019) 3D dust map that the emission north of $b \approx -12°$ in this arc is associated with a single, coherent structure at a distance of ∼530 pc—we interpret this as a shell ∼10 pc in radius. In Figure 4, we see that the H I in the velocity interval where we detect HCO^+ and SiO (−5 to 5 km s^{-1}; Table 4) obeys a similar arc-like morphology (HI4PI Collaboration et al. 2016). The CO in this direction is filamentary and relatively dense (Liszt & Pety 2012), with a moderately high excitation temperature ∼7 K (Liszt & Lucas 1998) as compared to similar sight lines. It is possible that turbulent flows driven by the expansion of the shell could contribute to these characteristics as well as to the formation of SiO in this direction.

4.1.5. NRAO 530

The sight line toward NRAO 530 intersects the outskirts of the Aquila molecular cloud, at a distance of ∼200 pc. The velocities of the HCO^+ and SiO features detected in this direction are consistent with their association with the Aquila molecular cloud (Dame et al. 2001). CO has been detected in emission (peak CO brightness temperature ≈0.5–0.6 K) and absorption (N(CO) ≈ 1.1 × 10^{15} cm^{-2}) in this direction (Liszt & Lucas 1998).

4.1.6. 4C+28.07

We detect HCO^+ at −6 and −1 km s^{-1} in the direction of 4C+28.07 (see Figure 1). The velocities of these features likely suggest an association with Perseus and Taurus, respectively. In Figure 1, it is clear that this sight line intersects the Per–Tau shell (Bialy et al. 2021), confirming the association. We find faint CO in this direction at -5 km s^{-1} $\lesssim v \lesssim$ 2 km s^{-1} (Dame & Thaddeus 2022).

4.1.7. 4C 09.57

We detect four HCO^+ components in this direction. All peaks are associated with peaks in H I emission, with the three highest-velocity components being associated with more diffuse H I than the lowest-velocity component. We find no CO emission in this direction (Planck Collaboration et al. 2014; Dame & Thaddeus 2022). In the 3D dust map from Leike et al. (2020), it is clear that this sight line passes through at least one bubble-like feature at a distance of around 100 pc, the far side of which accounts for the density peak at ∼150 pc and seems to be associated with the Local Bubble wall.

4.1.8. J0423-0120

We detect one HCO^+ absorption component and find no CO emission in this direction (Planck Collaboration et al. 2014; Dame & Thaddeus 2022). In the dust maps, there is a density peak at ∼150 pc, perhaps associated with the Local Bubble wall.

4.2. Density Constraints

We first attempt to find density estimates from the literature in the direction of our background sources. Araya et al. (2014) observed H_2CO in absorption in the directions of 3C 111 and BL Lac. They argued that the excitation temperature of H_2CO implies an upper limit to the density of $n_H < 10^5$ cm^{-3} in these directions, while the relatively weak absorption by H_2CO compared to CO and HCO^+ suggests that the density probably is $n_H \gtrsim 10^2$ cm^{-3}. Meanwhile, NRAO 530 lies in the outskirts of the Aquila molecular cloud. Denser clouds and molecular cores in Aquila have densities ∼10^4 cm^{-3} (Levshakov et al. 2013). Presumably the density toward NRAO 530 is significantly lower, as it is in the much more diffuse outskirts of Aquila. We therefore suggest 10^2 cm^{-3} $\lesssim n_H \lesssim$ 10^3 cm^{-2} (Snow & McCall 2006; Levshakov et al. 2013). The molecular absorption associated with the Perseus arm in the direction of 3C 418, where we detect SiO, is CO-dark at a sensitivity of ∼0.1 K (Dame et al. 2001). Busch et al. (2019) showed that CO-dark gas in the Perseus arm has densities $\lesssim$200 cm^{-3}. Given the low A_V (Snow & McCall 2006) and the absence of CO absorption and emission (see Figure 5 of Busch et al. 2019), we estimate that the density of the feature detected in SiO and HCO^+ absorption toward 3C 418 is $n_H \lesssim 200$ cm^{-3}. For other structures not explicitly discussed in previous works, we can use rough limits established for diffuse, translucent, and dense clouds (Snow & McCall 2006): $n_H \sim 10^4$ cm^{-3} for the structures in the direction of 2023+335 and 100 cm^{-3} $\lesssim n_H \lesssim 500$ cm^{-3} for the structures in the direction of 4C+28.07, 4C 09.57, and J0423-0120.

Alternatively, we can approximate the density of an interstellar structure by assuming some path length L,

$$n \approx \frac{N(\mathrm{H\,I}) + 2N(\mathrm{H_2})}{L}, \quad (2)$$

where N(H I) is the H I column density and $N(H_2)$ is the H_2 column density. We can estimate $N(H_2) \approx N(HCO^+)/3 \times 10^{-9}$ (see Section 3.4), where the HCO^+ column density is solved by integrating over the Gaussian feature (Equation (1)). N(H I) is more difficult to evaluate for individual structures because decomposing H I emission spectra into Gaussian components and matching those components to molecular absorption features is a complex process (e.g., Murray et al. 2018; Rybarczyk et al. 2022b). Nevertheless, we can estimate N(H I) using $N(\mathrm{H\,I}) = 1.823 \times 10^{18} \int T_B dv$ and by integrating over ±1 FWHM from the line center for each structure detected in absorption. Solving Equation (2) in this way, we find densities $n_H \sim$ 20–1500 cm^{-3} for $L = 1$ pc. In this case, only 2/31 structures have $n_H > 10^3$ cm^{-3}, while 27/31 structures have $n_H < 500$ cm^{-3}. Of course, these density estimates scale with $1/L$, and so would increase if we assume a smaller path length. For example, if we set L to the characteristic size of so-called "CO hot spots," clumps of enhanced CO emission in the diffuse/translucent ISM, then $L \sim 0.5$ pc and our density estimates increase by a factor of 2, which means that our estimates still largely fall in the range $n \sim 10^2$–10^3 cm^{-3}.

The local densities can also be constrained by the weakness of HCO^+ emission (e.g., Lucas & Liszt 1996; Liszt & Lucas 2000).

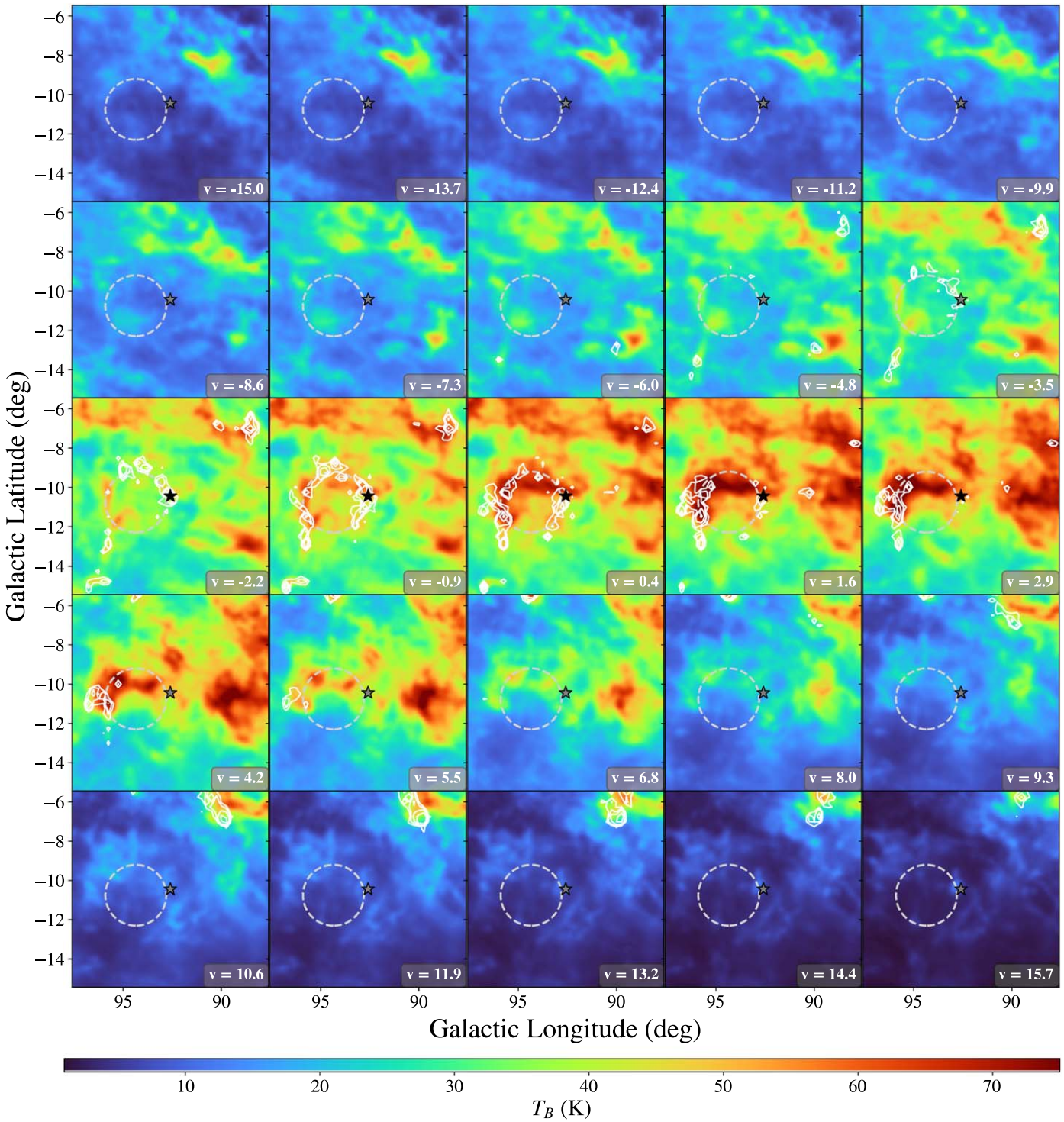

Figure 4. Maps of the H I emission (HI4PI Collaboration et al. 2016) in the direction of BL Lac. White contours of the CO emission (Dame & Thaddeus 2022) are shown at 0.25, 0.5, 1, and 2 K. The observed velocity of H I and CO is indicated in the bottom right corner of each panel. The position of BL Lac is indicated with a star, colored black and gray for velocities with and without detected HCO^+ absorption, respectively. The approximate boundary of the shell discussed in the text is shown as a dashed gray circle in all panels.

HCO^+ is detected in emission toward 3C 111 and BL Lac at levels of ∼0.04 K and ∼0.1 K, respectively (Lucas & Liszt 1996). While we are not aware of HCO^+ emission observations in the direction of our other background sources, sight lines with similar (or even slightly higher) A_V and integrated HCO^+ optical depths tend to show emission at $\lesssim$0.05 K, if detected at all (Lucas & Liszt 1996). While we do not have direct constraints on the kinetic temperature in most directions, the atomic hydrogen kinematically associated with HCO^+ and SiO absorption toward 3C 111 and BL Lac is ∼40–80 K, and more broadly the temperatures of H I structures kinematically associated with diffuse/translucent HCO^+ absorption are $\lesssim$80 K (Rybarczyk et al. 2022a). Given the HCO^+ column densities (Figure 5), optical depths (Table 2), low

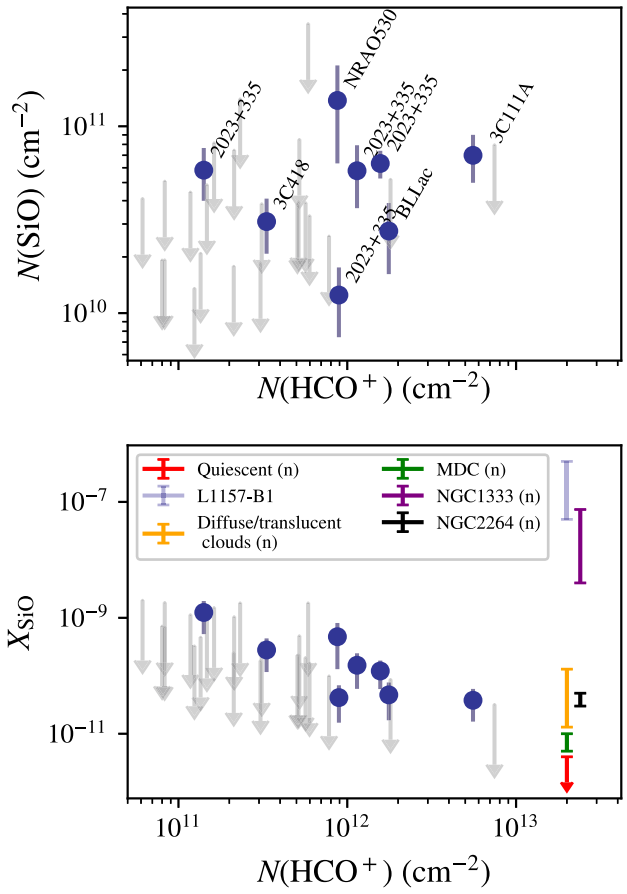

Figure 5. The SiO column density (top) and SiO abundance (bottom) vs. the HCO^+ column density for components identified in our Gaussian decomposition. For nondetections 3σ upper limits are shown in gray. Detections are shown in blue with 1σ error bars and are labeled in the top panel with the name of the background source against which each feature is detected (note the x-axes are the same in both panels). Previous SiO abundances measured in different interferometric experiments are shown for reference (Lucas & Liszt 2000; Duarte-Cabral et al. 2014; López-Sepulcre et al. 2016; Spezzano et al. 2020) (the x-axis values for these data are arbitrary). Results for narrow (FWHM $\lesssim 2$ km s^{-1}) SiO features are labeled "n" in the legend. Uncertainties in X_{SiO} include the uncertainty in $N(HCO^+)/N(H_2)$. We also show the estimated SiO abundance for quiescent gas measured in emission by Martin-Pintado et al. (1992) in red.

excitation temperatures (van der Tak et al. 2007; Godard et al. 2010; Luo et al. 2020), narrow line widths (Figure 6, Table 2), and estimated kinetic temperatures (Rybarczyk et al. 2022b), the weakness of the HCO^+ emission ($\lesssim$0.05 K) implies densities $\lesssim$ a few $\times 10^2$ cm^{-3} in most cases in our sample (van der Tak et al. 2007; Liszt 2020).

Taking into consideration the various approaches to estimating densities above, we put approximate limits on the densities in Table 5. These estimates are largely consistent, with typical densities $\sim 10^2$–10^3 cm^{-3}.

4.3. Estimating the Ages of Shells in H I and CO

As discussed above and seen in Figures 3 and 4, we find shells in CO (and H I in the case of BL Lac) where SiO absorption is detected. Here we estimate the ages of these shells.

The age of an expanding shell is $t_{exp} \approx \frac{2}{5}\frac{r}{v_{exp}}$, where v_{exp} is the expansion velocity and the factor of $2/5$ is appropriate for supernovae (Chevalier 1994). The California shell, observed here in the direction of 3C 111, has $r_{Cal} = 25$ pc. The Lacerta shell, observed here in the direction of BL Lac, has $r_{Lac} = 10$ pc. Because these sight lines are still within $\sim 10°$ of the Galactic plane, the H I emission is bright at these velocities, and it is difficult to isolate any double-peaked emission signature of the shells in H I to identify an expansion velocity (Ehlerová & Palouš 2005). If we assume a late-evolution expansion velocity of 8 km s^{-1} (e.g., Ehlerová & Palouš 2005), we find expansion times of 1.2 Myr and 0.5 Myr, respectively. We can also consider a broader range of expansion velocities, as expansion velocities of H I shells in the outer Galaxy have been found to range from $\sim$5 km s^{-1} to $\sim$25 km s^{-1} (Ehlerová & Palouš 2005). In this case, we find that the shells seen toward 3C 111 and BL Lac are $\sim$0.4–2 Myr and $\sim$0.2–0.8 Myr old, respectively.

5. High SiO Abundances in the Diffuse ISM

In Figure 5, we show the SiO column densities, N(SiO) (top panel), and abundances, X_{SiO} (bottom panel), for all components identified in the SiO absorption spectra. Where SiO is detected, X_{SiO} ranges from 3×10^{-11} to 1×10^{-9}. Our key result is that in all cases where we detect SiO, we find abundances a few to a few hundred times greater than those previously reported in quiescent environments, where $X_{SiO} \lesssim 4 \times 10^{-12}$ (Martin-Pintado et al. 1992). Quiescent clouds, which show no star formation activity, lack shocks with high enough velocities ($\sim$25 km s^{-1}) to sputter Si off the grain cores. In Figure 5 we compare our results with SiO abundances previously measured in high-resolution interferometric observations (Lucas & Liszt 2000; Duarte-Cabral et al. 2014; Spezzano et al. 2020; De Simone et al. 2022), as well as with the typically assumed quiescent abundance (Martin-Pintado et al. 1992). Our abundances in diffuse and translucent directions are higher than what was found in non-star-forming environments, and almost as high as what was reported in dense star-forming regions with powerful outflows.

Such high SiO abundances are difficult to explain when considering that our sight lines probe diffuse and translucent environments in the Milky Way: the three directions where we do not detect SiO have $A_V < 0.5$ mag, four of the directions where we detect SiO have 1 mag $< A_V <$ 5 mag, and only one direction where we detect SiO has $A_V > 5$ mag. Star formation in nearby clouds occurs only above a threshold of $A_V \sim 7$ mag (Lada et al. 2010). All our directions probe regions with extinction well below 7 mag, suggesting that it is unlikely for recent or ongoing star formation to be responsible for the formation of SiO. Studies of star formation in translucent clouds are rare, but several of these high-latitude clouds have no evidence of star formation (e.g., Hearty et al. 1999; Brand et al. 2012). Moreover, the densities of the absorbing structures along these lines of sight are $n \sim 10^2$–10^3 cm^{-3} in a large majority of cases (Section 4).

In two of the five directions where we detect SiO, the SiO appears to be associated with large, shell-like structures visible in CO (see Figures 3 and 4): the SiO in the direction of 3C 111A appears to be associated with the bubble on the eastern side of the California molecular cloud (Rezaei Kh. & Kainulainen 2022), while the SiO in the direction of BL Lac

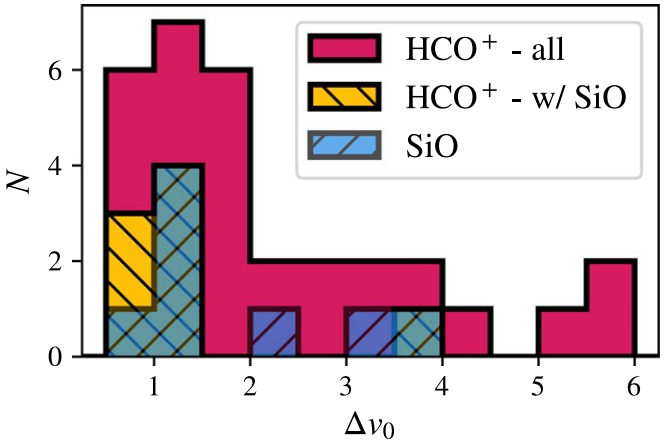

Figure 6. The distribution of FWHMs for Gaussian features identified in the HCO^+ absorption spectra and SiO absorption spectra. The unhatched dark pink histogram shows the distribution for all HCO^+ components, the diagonally hatched yellow histogram shows the distribution for HCO^+ components coincident with SiO absorption, and the blue diagonally hatched histogram shows the distribution for all SiO components.

is associated with a well-defined shell visible in both H I and CO, associated with the Lacerta molecular cloud (Figure 4; Dame et al. 2001; HI4PI Collaboration et al. 2016; Dame & Thaddeus 2022). The shells around 3C 111 and BL Lac do not appear particularly bright in Hα emission (Haffner et al. 2003, 2010) or in synchrotron or free–free emission (Planck Collaboration et al. 2016a)—the gas inside these shells is not highly ionized. Moreover, the faint Hα emission from diffuse and translucent structures could be largely caused by the scattering off of dust particles rather than by in situ ionized gas (Mattila et al. 2007; Lehtinen et al. 2010).

The absence of ongoing nearby star formation signatures in the directions of 3C 111A and BL Lac suggests that the shell-like structures are likely caused by a previous episode of star formation. Based on rough estimates of the expansion velocities, we suggest ages of ∼0.2–2 Myr for these shells. For comparison, the SiO abundances in recently shocked gas around star-forming regions are larger than $\sim 10^{-8}$ (e.g., Jiménez-Serra et al. 2010; Spezzano et al. 2020; De Simone et al. 2022), whereas the abundances measured toward BL Lac and 3C 111 are (3–5) $\times 10^{-11}$. Given the typical depletion time of SiO (Bergin et al. 1998; Codella et al. 1999), and especially considering the low densities observed here, it is plausible that the SiO absorption in these directions results from deaccelerated shocks in which the SiO has not yet been fully depleted/destroyed, or has been replenished through low-velocity shocks (Nguyen-Lu'o'ng et al. 2013).

Meanwhile, the remaining three sight lines with six SiO detections show no obvious shells/bubbles in H I and CO. NRAO 530 probes the far outskirts of the Aquila molecular cloud, 2023+335 intersects the Cygnus molecular cloud complex, and the SiO toward 3C 418 is clearly associated with the Perseus arm. In these directions, we have no evidence for active (or recently, within a few Myr, active) star formation. For example, if we isolate H I and H_2 (by proxy of HCO^+) from the Perseus arm in the direction of 3C 418, we find an optical extinction $0.3 \lesssim A_V \lesssim 0.6$, making it the most diffuse region where SiO has ever been detected in the ISM (Lucas & Liszt 2000; Corby et al. 2018). This is particularly interesting, as this feature has one of the highest SiO abundances in our sample, with $X_{SiO} \approx 2.8 \times 10^{-10}$. This is one of the highest SiO abundances ever detected in the diffuse/translucent ISM, and the highest detected where $A_V < 1$ mag. NRAO 530 and 2023 +335, while at higher visual extinction, have similarly high SiO abundances. Even in the absence of star formation or any clearly evident expanding structures, the diffuse and translucent gas in these directions has remarkably high SiO abundances compared to the typically assumed value in quiescent gas (Martin-Pintado et al. 1992).

Figure 6 shows the distribution of FWHMs for both the HCO^+ ($0.5\ \mathrm{km\,s^{-1}} < \mathrm{FWHM} < 5.8\ \mathrm{km\,s^{-1}}$) and SiO ($0.8\ \mathrm{km\,s^{-1}} < \mathrm{FWHM} < 3.9\ \mathrm{km\,s^{-1}}$) Gaussian absorption features. Such narrow line widths could allow us to exclude stellar outflows as a possible mechanism for SiO production. SiO lines are generally observed in protostellar outflows with a width of 20–50 $\mathrm{km\,s^{-1}}$ (Gueth et al. 1998; Nisini et al. 2007). In principle, SiO from a postshock layer could be associated with a line width of a few kilometers per second. However this line width is found only in small regions of protostellar outflows (see, e.g., Figure 7 of Gueth et al. 1998 or Figure 4 of Leurini et al. 2013), and it is rather unlikely that we catch only this component with our experiment. In our case, a protostellar outflow origin is all the less likely in that it is not compatible with the densities associated with our lines of sight (see Figure 1, Table 5, and related discussion below). We further note that the similarity in the line profiles of HCO^+ and SiO presented in Figure 2 and Table 2 could suggest that both species are formed under similar conditions (e.g., Schilke et al. 2001).

As shown in the top panel of Figure 5, the SiO column densities are relatively similar for structures with widely varying HCO^+ column densities. Under the assumption of a constant excitation temperature, the SiO column densities vary by a factor of 8, whereas the HCO^+ column densities vary by a factor of 38. This results in X_{SiO} decreasing with increasing HCO^+ column density, as seen in the bottom panel of Figure 5. If we fit a power law $X(\mathrm{SiO}) \propto N(\mathrm{HCO^+})^{\beta}$ to these points, we find $\beta = -1.29^{+0.48}_{-0.23}$, suggesting the decline is significant at a level $\sim 3\sigma$.

Six of the eight features with SiO detected have $N(\mathrm{HCO^+}) \gtrsim 10^{12}\ \mathrm{cm^{-2}}$, which is the column density at which Rybarczyk et al. (2022a) showed that equilibrium chemical models fail to explain the observed column densities of several molecular species, including HCO^+. In particular, Rybarczyk et al. (2022a) argued that nonequilibrium effects (i.e., shocks) are necessary to explain the HCO^+ column

densities and H I temperatures for features in the direction of 3C 111A and BL Lac, where indeed we detect SiO, and where there appears to be an association with dynamical processes (shell expansion from a previous generation of star formation). Meanwhile, only one of the structures with $N(HCO^+) > 10^{12}$ cm^{-2} has no detected SiO.[5] These observations provide direct evidence that the high observed column densities of several molecular species (e.g., HCO^+, HCN, C_2H, and HNC) in the diffuse ISM, which cannot be explained with equilibrium chemistry, are associated with dynamical events and shocks that trigger nonequilibrium chemistry (Godard et al. 2010; Rybarczyk et al. 2022a).

6. Discussion

Our results suggest that the formation of SiO in the diffuse ISM (i.e., in the absence of significant star formation and stellar feedback) is more widespread and effective than previously reported (Martin-Pintado et al. 1992). Even quiescent environments with $n < 10^3$ cm^{-3} can produce SiO with abundances similar to those found in much denser environments with $n > 10^4$ cm^{-3} (e.g., Duarte-Cabral et al. 2014; Louvet et al. 2016; De Simone et al. 2022) or in directions of protostellar outflows.

While explaining the origin of low-velocity shocks and SiO abundances in dense environments remains challenging, the SiO detections in diffuse regions that we report here are even harder to explain. The densities probed by our observations are most likely in the range 10^2–10^3 cm^{-3} (Section 4). Our results therefore challenge the current understanding of how shocks process dust grains and the distribution and form of silicon in the quiescent medium. What physical processes can form low-velocity shocks in the diffuse ISM remains an open question, though in the cases of 3C 111 and BL Lac, where shells are evident in H I and CO at velocities where we detect SiO, the SiO may be associated with expanding shells from old (∼0.2–2 Myr) star formation episodes.

We suggest that the typically assumed abundance of $X_{SiO} < 4 \times 10^{-12}$ for quiescent environments from Martin-Pintado et al. (1992) likely needs to be reconsidered. For example, we have detected SiO in perhaps the most diffuse environment to date—from the Perseus arm in the direction of 3C 418, where $n \sim 200$ cm^{-3}—which has an SiO abundance $X_{SiO} \approx 2.8 \times 10^{-10}$, almost 2 orders of magnitude higher than the typically assumed quiescent value. Abundances derived from interferometric observations offer a better measure of the local conditions along the line of sight than those derived from single-dish observations because of the much smaller beam size. Our absorption line observations against continuum sources trace a pencil beam, offering the best available measure of X_{SiO} in diffuse and translucent environments. Previous observations of SiO in environments with $n < 10^3$ cm^{-3} are exceedingly rare; while Lucas & Liszt (2000) hinted at elevated SiO abundances in diffuse and translucent environments, they did not investigate the abundances of individual structures (see Section 3.1) or find SiO at $A_V < 1.5$ mag. Our sample of SiO absorption from diffuse and translucent gas, the largest to date, clearly demonstrates that the SiO abundances in these environments do not align with the Martin-Pintado et al. (1992) result.

It is possible that a larger quantity of Si exists free in the gas phase or in dust grain mantles in the diffuse ISM than previously thought and/or that SiO is formed largely in purely gas-phase reactions. Models show that SiO column densities in low-velocity shocks are elevated by at least ∼3 orders of magnitude when 1%–10% of the preexisting (pre-shock) Si is in the gas phase[6] as compared to shocks where the Si is entirely locked in grain cores and mantles (for $n \sim 10^4$–10^5 cm^{-3}; Gusdorf et al. 2008; Lesaffre 2013; Nguyen-Lu'o'ng et al. 2013; Louvet et al. 2016). This suggested fraction of free Si from modeling is roughly consistent with observations (e.g., the heavy depletion case from Jenkins 2009; see their Equations (1) and (2) and Table 4). Moreover, SiO production by weak shocks may depend on the history of the gas—previous strong shocks may have released Si into the gas phase or moved Si from the grain cores to the grain surfaces, therefore making it easier for a subsequent generation of weaker shocks to produce SiO.[7] In this scenario, in regions with no history of strong shocks, one could expect that the observed SiO abundance falls toward lower values, which could provide an interpretation for the upper limits in abundance shown in Figure 5. Understanding the physical processes effective at releasing Si is essential for constraining dust grain destruction and accretion rates. We anticipate that mechanisms such as cloud–cloud collisions, ram pressure, and turbulent dissipation—all of which can occur in the diffuse ISM—may play a crucial role in the processing of dust grains and may provide the initial conditions for the earliest stages of molecule formation. These mechanisms need to be better understood and included in future numerical simulations of star formation and galaxy evolution.

Finally, the detection and high abundance of SiO in the diffuse and translucent environments observed here, especially in directions where there is no clear evidence for dynamical processes, may suggest that shocks are not the key vehicle for SiO production in at least some interstellar environments. For example, interstellar grains accelerated by MHD turbulence can be shattered (Jones et al. 1996) in grain–grain collisions at high speeds through gyroresonance interactions even in regions that are not shocked (Yan et al. 2004). Grains reach sufficiently high velocities to shatter even in the relatively diffuse cold neutral medium (Moseley et al. 2023). The Si released when UV radiation destroys shattered grains could contribute to the formation of SiO in such environments, eliminating the need for shocks to uniquely explain the formation of SiO. It has been argued that UV (and presumably X-rays and cosmic rays) can also release Si from grain cores (Schilke et al. 2001), and probably even more easily release it from grain mantles. The decrease in SiO with increasing HCO^+ column density may be in agreement with SiO originating in photodissociation regions (PDRs) as a result of the UV radiation field (Schilke et al. 2001), since the thickness of PDR layers does not depend on the total column density of the cloud. However, we expect relatively weak radiation fields in these directions compared to those in Schilke et al. (2001), and Rybarczyk et al. (2022a) argued against PDRs (based on the H I and HCO^+ properties) in at least two of the five directions where SiO is detected. With

[5] This is in the direction of 3C 111A; see Section 3.4 and Table 4 for further discussion.

[6] In these models SiO is removed from the gas phase by conversion to SiO_2 or reabsorption onto the surface of grains on a somewhat long timescale; see discussion in Gusdorf et al. (2008).

[7] We note that the path $SiO_2 + H \rightarrow SiO + OH$ does not likely contribute to the formation of SiO in these environments because the reaction is highly endothermic and the conditions in which this reaction could take place are not likely to occur.

future measurements, we will provide a more robust test of whether N(SiO) remains similar across diverse environments (Figure 5; see also Figure 8 of Schilke et al. 2001). While our results are important to clarify and inform the use of SiO as a shock tracer in the Milky Way and other galaxies, an understanding of additional chemical pathways effective in producing high SiO abundances purely from the gas-phase chemistry will require future studies and larger observational samples. Our future work will focus on a larger observational sample and detailed chemical modeling.

7. Conclusions

We have observed SiO in absorption in the direction of eight background continuum sources in diffuse and translucent directions. Though still modest, this represents the largest sample to date of SiO absorption in the diffuse and translucent ISM. These observations have important implications for the physics and chemistry of diffuse gas in the Milky Way.

1. We detect SiO in five of the eight directions, including all directions with $A_V \gtrsim 1$. For all structures detected in SiO absorption here, $A_V < 5$ mag, suggesting that these environments are all non-star-forming (Lada et al. 2010).
2. The observed line widths of the SiO absorption lines are narrow ($0.8\ \mathrm{km\,s^{-1}} < \mathrm{FWHM} < 3.9\ \mathrm{km\,s^{-1}}$), likely ruling out high-velocity shocks as a formation mechanism.
3. The SiO abundances we measure in the diffuse and translucent (non-star-forming) ISM are a few to a few hundred times greater than the typically assumed abundance in quiescent gas, $\lesssim 4 \times 10^{-12}$ (Martin-Pintado et al. 1992).
4. In at least two directions, SiO in the diffuse ISM is associated with shells visible in CO emission (and in H I emission in one case). We suggest that the SiO in these directions is associated with deaccelerated shocks from stellar feedback events 0.2–2 Myr ago.
5. SiO is detected in the two directions observed here where Rybarczyk et al. (2022a) showed that UV-dominated, equilibrium chemical models are unable to account for the high HCO^+ column densities. These are also the directions where shells are observed.
6. We emphasize the need for observational constraints on the distribution of Si in the gas phase and grain mantles, which are crucial for understanding the physics of grain processing and the chemistry in the ISM.

In this work, we have focused on observational constraints of the SiO abundance in the diffuse ISM. In upcoming work, we will use modeling to test the effectiveness of low-velocity shocks in the diffuse ISM in producing the SiO abundances observed here. Previous attempts to model low-velocity shocks have largely focused on denser environments (e.g., Nguyen-Lu'o'ng et al. 2013; Louvet et al. 2016) or have not directly modeled SiO emission or absorption (Lesaffre 2013). Future observations with NOEMA, ALMA, and JWST will also be critical for understanding the formation of SiO in both gas-phase and dust-enabled chemistry, as well as for modeling the earliest stages of molecule formation, which take place in the diffuse ISM.

We are grateful to Benjamin Godard, Bruce Draine, Guillaume Pineau des Forêts, Ana López-Sepulcre, Bob Benjamin, Jérôme Pety, and Maryvonne Gerin for helpful conversations about the interpretation of results presented here. We thank the anonymous referee for constructive comments. D.R.R. thanks Jan Martin Winters for support in the data reduction process. This work was supported by the University of Wisconsin–Madison Office of the Vice Chancellor for Research and Graduate Education with funding from the Wisconsin Alumni Research Foundation, the NSF Award AST-2108370, and the National Aeronautics and Space Administration under grant No. 4200766703. Support for this work was provided by the NSF through award SOSPA6-030 from the NRAO.

ORCID iDs

Daniel R. Rybarczyk https://orcid.org/0000-0003-3351-6831
Snežana Stanimirović https://orcid.org/0000-0002-3418-7817
Antoine Gusdorf https://orcid.org/0000-0002-0354-1684

References

Amo-Baladrón, M. A., Martín-Pintado, J., & Martín, S. 2011, A&A, 526, A54
Ando, R., Kohno, K., Tamura, Y., et al. 2016, PASJ, 68, 6
Araya, E. D., Dieter-Conklin, N., Goss, W. M., & Andreev, N. 2014, ApJ, 784, 129
Armijos-Abendaño, J., Banda-Barragán, W. E., Martín-Pintado, J., et al. 2020, MNRAS, 499, 4918
Bergin, E. A., Melnick, G. J., & Neufeld, D. A. 1998, ApJ, 499, 777
Bialy, S., Zucker, C., Goodman, A., et al. 2021, ApJL, 919, L5
Brand, J., Wouterloot, J. G. A., & Magnani, L. 2012, A&A, 547, A85
Busch, M. P., Allen, R. J., Engelke, P. D., et al. 2019, ApJ, 883, 158
Chen, W. P., & Lee, H. T. 2008, in Handbook of Star Forming Regions, Volume I, ed. B. Reipurth, Vol. 4 (San Francisco, CA: ASP), 124
Chevalier, R. A. 1994, in Supernovae, ed. S. A. Bludman, R. Mochkovitch, & J. Zinn-Justin (Amsterdam: Elsevier), 743
Codella, C., Bachiller, R., & Reipurth, B. 1999, A&A, 343, 585
Corby, J. F., McGuire, B. A., Herbst, E., & Remijan, A. J. 2018, A&A, 610, A10
Dame, T. M., Hartmann, D., & Thaddeus, P. 2001, ApJ, 547, 792
Dame, T. M., & Thaddeus, P. 2022, ApJS, 262, 5
de Geus, E. J., & Phillips, J. A. 1996, in IAU Symp. 169, Unsolved Problems of the Milky Way, ed. L. Blitz & P. J. Teuben (Dordrecht: Kluwer), 575
De Simone, M., Codella, C., Ceccarelli, C., et al. 2022, MNRAS, 512, 5214
Duarte-Cabral, A., Bontemps, S., Motte, F., et al. 2014, A&A, 570, A1
Ehlerová, S., & Palouš, J. 2005, A&A, 437, 101
Endres, C. P., Schlemmer, S., Schilke, P., Stutzki, J., & Müller, H. S. P. 2016, JMoSp, 327, 95
Gerin, M., Liszt, H., Neufeld, D., et al. 2019, A&A, 622, A26
Gildas Team 2013, GILDAS: Grenoble Image and Line Data Analysis Software, Astrophysics Source Code Library, ascl:1305.010
Godard, B., Falgarone, E., Gerin, M., Hily-Blant, P., & de Luca, M. 2010, A&A, 520, A20
Godard, B., Falgarone, E., & Pineau Des Forêts, G. 2009, A&A, 495, 847
Gong, M., Ostriker, E. C., Kim, C.-G., & Kim, J.-G. 2020, ApJ, 903, 142
Gueth, F., Guilloteau, S., & Bachiller, R. 1998, A&A, 333, 287
Gusdorf, A., Cabrit, S., Flower, D. R., & Pineau Des Forêts, G. 2008, A&A, 482, 809
Haffner, L. M., Reynolds, R. J., Madsen, G. J., et al. 2010, in ASP Conf. Ser. 438, The Dynamic Interstellar Medium: A Celebration of the Canadian Galactic Plane Survey, ed. R. Kothes, T. L. Landecker, & A. G. Willis (San Francisco, CA: ASP), 388
Haffner, L. M., Reynolds, R. J., Tufte, S. L., et al. 2003, ApJS, 149, 405
Han, J., Yun, Y., & Park, Y.-S. 2017, JKAS, 50, 185
Hatchell, J., Fuller, G. A., & Millar, T. J. 2001, A&A, 372, 281
Hearty, T., Magnani, L., Caillault, J. P., et al. 1999, A&A, 341, 163
Herbst, E., Millar, T. J., Wlodek, S., & Bohme, D. K. 1989, A&A, 222, 205
HI4PI Collaboration, Ben Bekhti, N., Flöer, L., et al. 2016, A&A, 594, A116
Hopkins, P. F., Quataert, E., & Murray, N. 2012, MNRAS, 421, 3488
Jenkins, E. B. 2009, ApJ, 700, 1299
Jiménez-Serra, I., Caselli, P., Tan, J. C., et al. 2010, MNRAS, 406, 187
Jones, A. P., Tielens, A. G. G. M., & Hollenbach, D. J. 1996, ApJ, 469, 740

Lada, C. J., Lewis, J. A., Lombardi, M., & Alves, J. 2017, A&A, 606, A100
Lada, C. J., Lombardi, M., & Alves, J. F. 2010, ApJ, 724, 687
Lallement, R., Babusiaux, C., Vergely, J. L., et al. 2019, A&A, 625, A135
Lehtinen, K., Juvela, M., & Mattila, K. 2010, A&A, 517, A79
Leike, R. H., Glatzle, M., & Enßlin, T. A. 2020, A&A, 639, A138
Lesaffre, P., Pineau des Forêts, G., Godard, B., et al. 2013, A&A, 550, A106
Leurini, S., Codella, C., Gusdorf, A., et al. 2013, A&A, 554, A35
Levshakov, S. A., Henkel, C., Reimers, D., et al. 2013, A&A, 553, A58
Li, S., Wang, J., Fang, M., et al. 2019, ApJ, 878, 29
Liszt, H. 2001, A&A, 370, 576
Liszt, H., & Gerin, M. 2023, ApJ, 943, 172
Liszt, H., Gerin, M., & Grenier, I. 2018, A&A, 617, A54
Liszt, H., & Lucas, R. 2000, A&A, 355, 333
Liszt, H. S. 2020, ApJ, 897, 104
Liszt, H. S., & Lucas, R. 1998, A&A, 339, 561
Liszt, H. S., & Pety, J. 2012, A&A, 541, A58
Liszt, H. S., Pety, J., Gerin, M., & Lucas, R. 2014, A&A, 564, A64
Liszt, H. S., Pety, J., & Lucas, R. 2010, A&A, 518, A45
López-Sepulcre, A., Watanabe, Y., Sakai, N., et al. 2016, ApJ, 822, 85
Louvet, F., Motte, F., Gusdorf, A., et al. 2016, A&A, 595, A122
Lucas, R. 1998, A&A, 337, 246
Lucas, R., & Liszt, H. 1996, A&A, 307, 237
Lucas, R., & Liszt, H. S. 2000, A&A, 355, 327
Luo, G., Li, D., Tang, N., et al. 2020, ApJL, 889, L4
Martin-Pintado, J., Bachiller, R., & Fuente, A. 1992, A&A, 254, 315
Martín-Pintado, J., de Vicente, P., Fuente, A., & Planesas, P. 1997, ApJL, 482, L45
Mattila, K., Juvela, M., & Lehtinen, K. 2007, ApJL, 654, L131
McKee, C. F., & Ostriker, J. P. 1977, ApJ, 218, 148
Moseley, E. R., Teyssier, R., & Draine, B. T. 2023, MNRAS, 518, 2825
Müller, H. S. P., Thorwirth, S., Roth, D. A., & Winnewisser, G. 2001, A&A, 370, L49
Murray, C. E., Stanimirović, S., Goss, W. M., et al. 2018, ApJS, 238, 14
Nguyen-Lu'o'ng, Q., Motte, F., Carlhoff, P., et al. 2013, ApJ, 775, 88
Nisini, B., Codella, C., Giannini, T., et al. 2007, A&A, 462, 163
Pety, J. 2005, in SF2A-2005: Semaine de l'Astrophysique Francaise, ed. F. Casoli et al. (Les Ulis: EDP Sciences), 721
Planck Collaboration, Adam, R., & Ade, P. A. R. 2016a, A&A, 594, A10
Planck Collaboration, Ade, P. A. R., Aghanim, N., et al. 2014, A&A, 571, A13
Planck Collaboration, Aghanim, N., Ashdown, M., et al. 2016b, A&A, 596, A109
Reach, W. T., & Heiles, C. 2021, ApJ, 909, 71
Rezaei Kh., S., & Kainulainen, J. 2022, ApJL, 930, L22
Rivilla, V. M., Jiménez-Serra, I., Zeng, S., et al. 2018, MNRAS, 475, L30
Rybarczyk, D. R., Gong, M., Stanimirović, S., et al. 2022a, ApJ, 926, 190
Rybarczyk, D. R., Stanimirović, S., Gong, M., et al. 2022b, ApJ, 928, 79
Schilke, P., Pineau des Forêts, G., Walmsley, C. M., & Martín-Pintado, J. 2001, A&A, 372, 291
Schilke, P., & Walmsley, C. M. 1997, A&A, 321, 293
Schöier, F., van der Tak, F., van Dishoeck, E., & Black, J. 2010, LAMDA: Leiden Atomic and Molecular Database, Astrophysics Source Code Library, ascl:1010.077
Snow, T. P., & McCall, B. J. 2006, ARA&A, 44, 367
Spezzano, S., Codella, C., Podio, L., et al. 2020, A&A, 640, A74
Turner, B. E. 1998, ApJ, 495, 804
van der Tak, F. F. S., Black, J. H., Schöier, F. L., Jansen, D. J., & van Dishoeck, E. F. 2007, A&A, 468, 627
Wiklind, T., & Combes, F. 1997, A&A, 324, 51
Yan, H., Lazarian, A., & Draine, B. T. 2004, ApJ, 616, 895
Yu, N.-P., Xu, J.-L., & Wang, J.-J. 2018, RAA, 18, 015
Zhu, H., Tian, W., Li, A., & Zhang, M. 2017, MNRAS, 471, 3494